TU/e EINDHOVEN UNIVERSITY OF TECHNOLOGY

Plasma-Assisted ALD of Highly Conductive HfNx: On the Effect of Energetic Ions on Film Microstructure

Citation for published version (APA):
Karwal, S., Verheijen, M. A., Arts, K., Faraz, T., Kessels, W. M. M., & Creatore, M. (2020). Plasma-Assisted ALD of Highly Conductive HfNx: On the Effect of Energetic Ions on Film Microstructure. *Plasma Chemistry and Plasma Processing*, *40*(3), 697-712. https://doi.org/10.1007/s11090-020-10079-x

DOI:
10.1007/s11090-020-10079-x

Document status and date:
Published: 01/05/2020

Document Version:
Publisher's PDF, also known as Version of Record (includes final page, issue and volume numbers)

Please check the document version of this publication:

• A submitted manuscript is the version of the article upon submission and before peer-review. There can be important differences between the submitted version and the official published version of record. People interested in the research are advised to contact the author for the final version of the publication, or visit the DOI to the publisher's website.
• The final author version and the galley proof are versions of the publication after peer review.
• The final published version features the final layout of the paper including the volume, issue and page numbers.

Link to publication

General rights
Copyright and moral rights for the publications made accessible in the public portal are retained by the authors and/or other copyright owners and it is a condition of accessing publications that users recognise and abide by the legal requirements associated with these rights.

• Users may download and print one copy of any publication from the public portal for the purpose of private study or research.
• You may not further distribute the material or use it for any profit-making activity or commercial gain
• You may freely distribute the URL identifying the publication in the public portal.

If the publication is distributed under the terms of Article 25fa of the Dutch Copyright Act, indicated by the "Taverne" license above, please follow below link for the End User Agreement:

www.tue.nl/taverne

Take down policy
If you believe that this document breaches copyright please contact us at:

openaccess@tue.nl

providing details and we will investigate your claim.

Download date: 04. Oct. 2023

Plasma Chemistry and Plasma Processing (2020) 40:697–712
https://doi.org/10.1007/s11090-020-10079-x

ORIGINAL PAPER

Plasma-Assisted ALD of Highly Conductive HfN_x: On the Effect of Energetic Ions on Film Microstructure

Saurabh Karwal[1] · Marcel A. Verheijen[1,2] · Karsten Arts[1] · Tahsin Faraz[1] · Wilhelmus M. M. Kessels[1] · Mariadriana Creatore[1]

Received: 26 September 2019 / Accepted: 23 March 2020 / Published online: 13 April 2020
© The Author(s) 2020

Abstract
In this work, we report on the atomic layer deposition (ALD) of HfN_x thin films by employing $CpHf(NMe_2)_3$ as the Hf(IV) precursor and Ar–H_2 plasma in combination with external RF substrate biasing as the co-reactant. Following up on our previous results based on an H_2 plasma and external RF substrate biasing, here we address the effect of ions with a larger mass and higher energy impinging on HfN_x film surface during growth. We show that an increase in the average ion energy up to 304 eV leads to a very low electrical resistivity of 4.1×10^{-4} Ωcm. This resistivity value is achieved for films as thin as ~35 nm, and it is an order of magnitude lower than the resistivity reported in literature for HfN_x films grown by either CVD or ALD, while being comparable to the resistivity of PVD-grown HfN_x films. From the extensive thin film characterization, we conclude that the impinging ions during the film growth lead to the very low electrical resistivity of HfN_x films by suppressing the oxygen incorporation and in-grain nano-porosity in the films.

Keywords Atomic layer deposition · Hafnium nitride · RF substrate bias · Electrical conductivity

Introduction

Conductive transition metal nitride (TMN) films find many applications in nano-electronics. They are used as metal electrodes in metal oxide semiconductor field effect transistors (MOSFETs) [1–4], and as diffusion barriers in inter-connects [5–8]. In view of the continuous scaling of semiconductor devices, the application of TMN films at small dimensions requires ultra-thin films with low resistivity, besides forming stable interfaces, e.g. with the

Electronic supplementary material The online version of this article (https://doi.org/10.1007/s11090-020-10079-x) contains supplementary material, which is available to authorized users.

✉ Mariadriana Creatore
m.creatore@tue.nl

[1] Department of Applied Physics, University of Technology Eindhoven, P.O. Box 513, 5600MB Eindhoven, Netherlands

[2] Eurofins Material Science, High Tech, Campus 11, 5656 AE Eindhoven, The Netherlands

underlying high-k HfO_2 [1, 3, 4, 8]. Specifically, thin films of titanium nitride and tantalum nitride tend to form undesirable oxy-nitrides at the interface with HfO_2 [4, 8]. Low resistivity hafnium nitride (HfN_x) can serve as an effective alternative because of its superior stability when used in combination with HfO_2 [8].

HfN_x predominantly exists in two crystal phases: highly resistive Hf_3N_4 with Hf(IV) oxidation state [9, 10], and low resistivity δ-HfN with Hf(III) oxidation state [11, 12]. The control of the oxidation state of Hf is therefore essential to synthesize conductive HfN_x layers [13–15]. Physical vapor deposition (PVD) methods have been widely adopted for the synthesis of low resistivity HfN_x films [8, 11, 12, 16–19]. Seo et al. have reported the growth of stoichiometric and epitaxial 500 nm thick HfN_x layers with a resistivity of 1.4×10^{-5} Ωcm, which is the lowest resistivity value reported thus far [18]. Typically, the polycrystalline HfN_x films prepared by PVD exhibit a resistivity of ca. $(1–2)\cdot10^{-4}$ Ωcm for a typical film thickness of ~ 200 nm [17, 19, 20]. On the other hand, the growth of low resistivity HfN_x films by techniques employing a metal–organic precursor, such as chemical vapor deposition (CVD) or atomic layer deposition (ALD), is very challenging [13, 14, 21–23]. A major challenge is the reduction of Hf(IV) oxidation state in the precursor to Hf(III) oxidation state in the deposited film, as highlighted in our previous work [13, 14]. Kim et al. reported the growth of HfN_x films with a resistivity of 1×10^{-3} Ωcm, the lowest achieved by means of CVD [21].

The urgent requirement from the field of nano-electronics is the synthesis of ultra-thin films with precise control over film thickness, excellent uniformity and conformality on high aspect ratio 3D nanostructures [24–27]. These requirements motivate the synthesis of low resistivity HfN_x films by ALD. We have recently shown that the δ-HfN phase can be achieved by adopting $CpHf(NMe_2)_3$ as Hf(IV) precursor and H_2 plasma as reducing co-reactant in a plasma-assisted ALD process [13]. We demonstrated that the application of an external RF substrate bias during the H_2 plasma exposure and an increase in the time-averaged substrate potential ($|V_{bias}|$) from 0 to 130 V resulted in a major decrease in electrical resistivity (ρ_e) from 0.9 to 3.3×10^{-3} Ωcm [14]. The decrease in ρ_e was found to be correlated with a major increase in the fraction of Hf(III) oxidation state from 0.65 ± 0.02 to 0.82 ± 0.02 [13, 14]. These results demonstrated that the impingement of energetic ions during the film growth can significantly improve the chemical and associated electrical properties of HfN_x thin films prepared by ALD. In parallel, Villamayor et al. recently showed that an increase in the mass of impinging ions positively affects also the crystallinity of HfN_x films grown by PVD, which contributes to the decrease in electrical resistivity [20].

In the present work, we investigate the effect of Ar–H_2 plasma in combination with external RF substrate biasing during the plasma half cycle as the reducing co-reactant. The impact of impingement of ions with larger mass and higher energy on the chemical and microstructural properties of HfN_x films is addressed here. The motivation to use Ar–H_2 plasma derives from the work of Sode et al. [28]. ArH^+ is anticipated to be the most abundant ion in an Ar–H_2 plasma, in contrast to the lighter H_3^+ ion in a H_2 plasma as employed in the previous work [28]. Furthermore, the ion energy measurements carried out in the present work indicate that the growing HfN_x film is subjected to a higher average ion energy ($<E_{ion}>$) in the case of Ar–H_2 plasma with respect to the previously reported H_2 plasma process [14]. The ions with a larger mass and higher $<E_{ion}>$ leads to a minimum in the electrical resistivity of 4.1×10^{-4} Ωcm. To best of our knowledge, this value represents the lowest resistivity reported in the literature for HfN_x films grown by either CVD or ALD, and is comparable to the resistivity of PVD grown films [13, 14, 21–23]. This low resistivity is achieved for films as thin as ~ 35 nm. As a result of impinging ions with a

larger mass and higher $<E_{ion}>$, a high Hf(III) fraction of 0.86 is obtained and major suppression of in-grain nano-porosity is observed, in contrast to the H_2 plasma process.

Experimental Section

Plasma-Assisted ALD of HfN_x

The ALD of HfN_x thin films was conducted in an Oxford Instruments FlexAL ALD reactor [14, 29, 30], equipped with an inductively coupled remote plasma (ICP) source with an alumina dielectric tube. The reactor chamber was pumped to a base pressure of 10^{-6} Torr using a turbo-molecular pump before every deposition. A stage temperature of 450 °C was selected for HfN_x ALD. This corresponds to a substrate temperature of about 340 °C as verified by spectroscopic ellipsometry (SE) [13, 14]. The onset of precursor decomposition and the start of a CVD regime was observed above 450 °C as previously reported [14]. The reactor walls were kept at 145 °C during all the depositions.

The Hf precursor $CpHf(NMe_2)_3$ (Air Liquide, > 99.99% purity) was contained in a stainless steel bubbler at 60 °C and bubbled by an Ar flow of 100 sccm. An Ar flow of 100 sccm was also injected into the ICP alumina tube during the precursor dosage in order to suppress deposition on the ICP tube walls (a gate valve present between the ICP source and reactor chamber was kept open during the full cycle). Following the precursor dose, the chamber was pumped down to a base pressure of 10^{-6} Torr in order to remove the unreacted precursor and reaction byproducts for 4 s. For the plasma exposure half cycle, an $Ar + H_2$ gas mixture (10 sccm Ar and 40 sccm H_2) was introduced into the chamber from the ICP alumina tube. The valve to the pump was fully opened culminating in a reactor pressure of ~ 6 mTorr. After stabilization of the gas flows for 4 s, the plasma was ignited with 100 W radio frequency (rf) ICP power (13.56 MHz) for the desired time. The purge steps for both half cycles consisted of a flow of 200 sccm Ar through the bubbling lines in addition to the 100 sccm Ar flow from the ICP source and with the valve to the pump fully opened. A $CpHf(NMe_2)_3$ pulse length of 4 s and plasma exposure of 10 s were used, while keeping the purge step of 2 s after every half cycle [13].

External RF Substrate Biasing

Employing the special feature of our Oxford Instruments FlexAL systems, an external substrate bias is applied during the plasma half cycle for the last 5 s using an additional RF power source (13.56 MHz), attached to the substrate table [14]. As a result, a time-averaged negative substrate potential with respect to ground (V_{bias}) develops during the plasma exposure [14]. The magnitude of V_{bias} is tuned by changing the applied RF power as previously reported in detail (supporting information, Figure AI) [14]. An oscilloscope was connected to the substrate table via a high voltage probe that was used to measure the RF bias voltage waveforms as a function of time [14]. Supporting information Figure AI also shows the $|V_{bias}|$ values for the applied RF bias power values [14, 31].

The ions are accelerated towards the surface of the growing film as a consequence of the voltage drop over the plasma sheath [31]. The ion flux-energy distribution functions (IFEDFs) of incident ions are measured using an Impedans Semion retarding field energy analyzer (RFEA) [31–33], as described in detail in Ref. [34]. As reported by Profijt et al., a mono-modal IFEDF for the grounded electrode ($|V_{bias}| = 0$ V) condition, whereas the

application of external RF substrate bias resulted in a bi-modal IFEDF [31]. The shape of the IFEDF for a collisionless sheath is determined by the ratio of ion transit time to the period of RF cycle [32]. The mean ion energy is denoted by E_{ion}, while ΔE_{ion} represents the peak-to-peak separation in a bimodal IFEDF in the text. Furthermore, the RFEA is also used to estimate the flux of incident ions using $\Gamma_i = I_c / e \cdot A_e$, where I_c is the collector current measured by the RFEA, e is the elementary charge and A_e is the effective collector area. Ref [34]. describes a detailed procedure to deduce the value of factor A_e, equal to $(3.9 \pm 1.0)\ 10^{-3}\ cm^2$ for the RFEA probe used in this work. Moreover, a slightly lower value of $|V_{bias}|$ was obtained during the IFEDF measurements using RFEA than during the growth of HfN_x films on a substrate, for a particular RF bias power application (supporting information, Figure AIc).

Substrates and Material Characterization

The HfN_x films are deposited on planar Si(100) substrates with a diameter of 100 mm and with 450 nm SiO_2 atop.

The growth per cycle (GPC) and the dielectric functions of the HfN_x films were examined using spectroscopic ellipsometry (SE, J.A. Woollam, Inc., M2000U). The dielectric functions ($0.75 \le h\nu \le 5.0$ eV) of HfN_x films could be modelled using one Drude and two Lorentz oscillators as demonstrated by Hu et al. (supporting information, Table AI for details and discussion on the selected optical model) [11]. Additionally, the optical film resistivity (ρ_{op}) was deduced from the free-carrier Drude parameterization, given by $\rho_{op} = (\Gamma_D / \varepsilon_o) \cdot \omega_p^2$, where Γ_D is the damping factor for the Drude oscillator, ε_o is the permittivity of free space, and ω_p is the screened plasma frequency. The electrical resistivity (ρ_e) was obtained via the four-point probe measurements using a Keithley 2400 SourceMeter and a Signaton probe by multiplying the sheet resistance of the HfN_x films with the film thickness as derived from SE. All resistivities reported in this work are for room temperature.

X-ray photoelectron spectroscopy (XPS) measurements were performed using a Thermoscientific K-Alpha KA1066 system equipped with a monochromatic Al Kα ($h\nu = 1486.6$ eV) source in order to study the chemical bonding and the oxidation states of elements present in the film. The chemical composition and the mass density of the films was evaluated via Rutherford backscattering spectrometry (RBS) and elastic recoil detection (ERD) using 1900 keV$^4He^+$ ions (Detect99). For the ERD measurements, the recoil angle was 30° and the angle of incidence with the sample surface was kept at 15° whereas for the RBS, two detectors were used with scattering angles of 170° and 150°.

The surface morphology and the lateral grain sizes of thick HfN_x films ($t > 30$ nm) were studied using a Zeiss Sigma field emission scanning electron microscope (FE-SEM) operated at an acceleration voltage of 2 kV.

The crystallinity of the HfN_x films was examined with a PANalytical X'pert PRO MRD X-ray diffractometer using a Cu Kα ($\lambda = 1.542$ Å) X-ray source. The X-ray diffractograms were obtained in a $\theta - 2\theta$ configuration and were compared with the powder HfN patterns [35, 36]. High-angle annular dark-field scanning transmission electron microscopy (HAADF-STEM) studies were conducted using a JEOL ARM 200F operated at 200 kV in order to analyze: (1) the lateral grain sizes of thin HfN_x films ($t \le 10$ nm), defined by the low atomic density grain boundary regions in the top-view images and (2) the microstructure and the nano-porosity of thick HfN_x films ($t > 30$ nm), obtained from the cross-sectional samples. These cross-sectional samples were prepared using a Focused Ion Beam

(FIB), following a standard lift-out sample preparation procedure. Prior to FIB milling, a protective layer was deposited on the HfN_x layers. In case of the Ar–H_2 plasma sample, a stack of Electron Beam Induced Deposited (EBID) SiO_2, EBID Pt/C and Ion Beam Induced Deposited (IBID) Pt was used. In case of the H_2 plasma sample, only EBID Pt/C and IBID Pt was used, as can be recognized from the TEM images below.

Results and Discussion

Ion Energy Characterization

The IFEDF measurements were carried out at various values of $|V_{bias}|$ for Ar–H_2 plasma and are presented in Fig. 1. The IFEDFs for the H_2 plasma process were also measured and are shown for comparison. It is noted that the energy distribution of ions with a specific mass cannot be resolved and rather a cumulative distribution of all the ions impinging on the surface is obtained. However, from literature [37–39] and a recent report from Sode et al. [28], it can be expected that an Ar–H_2 plasma contains ArH^+, Ar^+, H_3^+, H_2^+ and H^+ ions, with ArH^+ being the most abundant ion under a similar experimental conditions. In a pure H_2 plasma discharge, H_3^+ is the most abundant ion, in combination with H_2^+ and H^+ ions [28].

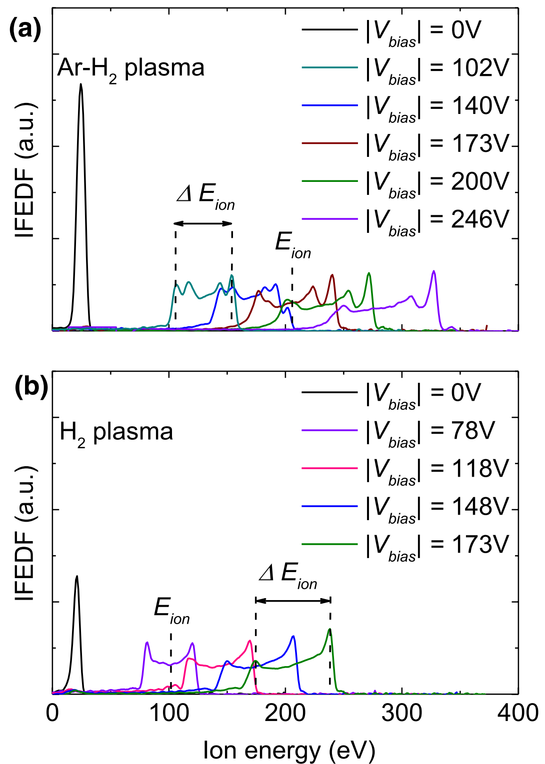

Fig. 1 Ion flux-energy distribution functions (IFEDFs) for ions in a **a** Ar–H_2 plasma operated at 6 mTorr and **b** H_2 plasma operated at 30 mTorr for various values of $|V_{bias}|$

A mono-modal IFEDF with an average ion energy ($<E_{ion}>$) of 24 eV was obtained for the grounded electrode ($|V_{bias}|=0$ V) for the Ar–H_2 plasma as shown in Fig. 1a. The application of 10 W RF bias power resulted in an asymmetrical IFEDF with a $|V_{bias}|=102$ V, $<E_{ion}>=126$ eV and an outermost peak-to-peak width (ΔE_{ion}) of 47 eV. Upon increasing the RF bias power to 60 W, the value of $|V_{bias}|$ increased to 246 V, the $<E_{ion}>$ increased to 308 eV and an ΔE_{ion} of 77 eV was obtained. The increase in ΔE_{ion} with $|V_{bias}|$ is a consequence of an increase in the peak-to-peak sheath voltage [32]. Furthermore, when closely inspecting the IFEDFs, they appear to be a superposition of multiple bi-modal IFEDFs of individual cationic species with different masses (i.e. ArH^+, Ar^+, H_3^+, H_2^+ and H^+), that have different transit times through the plasma sheath as described by Manenschijn et al. [40]. This may be expected at low operating pressures used, where there are less ion-neutral collisions in the plasma sheath and ions are essentially unidirectional towards the surface of growing film.

Figure 1b shows the IFEDFs at various values of $|V_{bias}|$ for the previously reported H_2 plasma process at 30 mTorr. Similar to the Ar–H_2 plasma, a mono-modal IFEDF was obtained for the grounded electrode ($|V_{bias}|=0$ V), centered at $<E_{ion}>$ of 19 eV. Upon the application of external RF substrate bias, the IFEDF became bi-modal and an $<E_{ion}>$ of 98 eV with ΔE_{ion} of 39 eV was obtained at $|V_{bias}|=78$ V (rf bias power = 10 W). Furthermore, the $<E_{ion}>$ and ΔE_{ion} increases with $|V_{bias}|$ in a similar fashion as for Ar–H_2 plasma.

The flux of impinging ions (Γ_i) was calculated from the total ion current (I_c) recorded by the RFEA, since the flux of impinging ions is also expected to influence the film growth and related properties, as shown by Adibi et al. [41]. In our case, a constant Γ_i of $(9.0 \pm 2.1)\cdot 10^{14}$ cm^{-2} s^{-1} was calculated independent of $|V_{bias}|$ for the Ar–H_2 plasma, whereas a slight increase in Γ_i from $(3.1 \pm 0.7)\cdot 10^{14}$ cm^{-2} s^{-1} at $|V_{bias}|=0$ V to $(9.5 \pm 2.2)\cdot 10^{14}$ cm^{-2} s^{-1} at $|V_{bias}|=173$ V was observed for the H_2 plasma process. Based on these results, we can conclude that the values of Γ_i for both the processes are relatively similar in the entire range of $|V_{bias}|$ investigated, whereas a significant increase in E_{ion} is observed in the case of the Ar–H_2 plasma.

Opto-Electrical Properties of HfN_x

The ALD process was extensively characterized in terms of growth-per-cycle (GPC) and material properties. A detailed discussion can be found in the supporting information and here, only a few aspects are highlighted. The GPC was found to be constant at 0.35 ± 0.04 Å/cycle (supporting information Figure AIII), independent of the increase in the $|V_{bias}|$ from 0 to 255 V. Above the $|V_{bias}|$ value of 255 V, a slight increase in the GPC was observed. The previously reported data for the H_2 plasma process is also included in supporting information Figure AIII for comparison. Furthermore, based on our previous studies on the ALD process employing H_2 plasma, it is anticipated that the application of external RF substrate bias does not affect the saturation behavior of the ALD process [14].

Figure 2a shows the ρe and the ρ_{op} resistivity values for HfN_x films as a function of $|V_{bias}|$. The HfN_x films grown at $|V_{bias}|=0$ V using an Ar–H_2 plasma exhibit values of ρ_e of (2.0 ± 0.1) 10^{-1} Ωcm and of $\rho_{op}=(5.2 \pm 0.1)$ 10^{-3} Ωcm. When increasing the $|V_{bias}|$ value up to 255 V, a substantial decrease in ρ_e to (4.1 ± 0.1) 10^{-4} Ωcm and in ρ_{op} to (2.4 ± 0.1) 10^{-4} Ωcm was observed. A subsequent increase in $|V_{bias}|$ value to 367 V led to an increase in ρ_e to $(6.5 \pm 0.1)\cdot 10^{-4}$ Ωcm and ρ_{op} to $(3.5 \pm 0.1)\cdot 10^{-4}$ Ωcm. Figure 2a

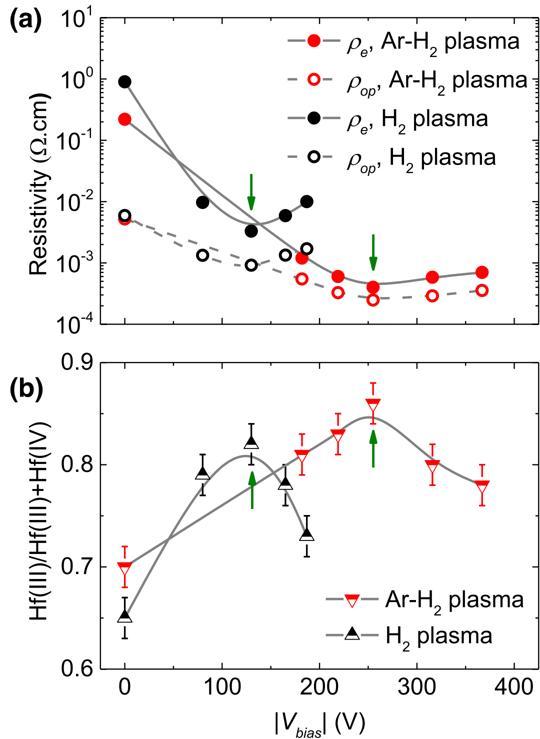

Fig. 2 **a** Electrical (ρ_e) and optical resistivity (ρ_{op}) values for ~ 35 nm HfN_x films grown using Ar–H_2 plasma compared with previously reported ~ 80 nm HfN_x films grown using H_2 plasma and **b** the corresponding Hf(III) oxidation state fractions as a function of $|V_{bias}|$. Lines serve as a guide to the eye and the (green) arrows indicate the *optimum condition* in terms of minimum in resistivity achieved in both ALD processes (Color figure online)

also contains the previously reported ρ_e and ρ_{op} data for the H_2 plasma process for comparison [14].

It should be noted that the very low ρ_e achieved at $|V_{bias}|$ = 255 V is for HfN_x films as thin as ~ 35 nm. To best of our knowledge, this resistivity value is the lowest reported for HfN_x films grown by either CVD or ALD, and is comparable to values reported for PVD-grown films [13, 14, 21–23]. The $|V_{bias}|$ value that yields the minimum in ρ_e and ρ_{op} is here referred to as *optimum condition* for the corresponding ALD process and the rest of the manuscript will address the film characterization mainly at the optimum conditions.

By considering that the interaction distance of the incident light with the HfN_x films is rather small, it can be expected that only the crystalline quality within 3–4 nm is probed by SE for determining the ρ_{op} (see Table AI and the discussion underneath). Therefore, the difference between the ρ_e and ρ_{op} (Δ_ρ) provides insights into the amount of electronic scattering in the HfN_x films, as we previously described [13, 14, 42]. A very low Δ_ρ is achieved at the optimum condition for Ar–H_2 plasma. It is relevant here to underline that Δ_ρ is an order of magnitude smaller than in the case of the previously reported H_2 plasma process. This suggests that the application of Ar–H_2 plasma has greatly contributed to reduce the amount of electronic scattering in the HfN_x films. In order to comprehend the reason behind the very low scattering and the low value of ρ_e achieved at the optimum condition, the chemical composition and microstructure of the HfN_x films was studied [14].

Chemical Properties of HfN_x

The chemical composition of the HfN_x films was investigated by means of XPS and RBS. The binding energy values attributed to each spectral line for a specific chemical element in the XPS spectrum can be found in the supporting information (Table AII). Figure 2b shows the Hf(III) oxidation state fraction as a function of $|V_{bias}|$. For comparison, the previously reported Hf(III) fraction data for H_2 plasma is also shown. The Hf(III) fraction increased from 0.70 ± 0.02 to 0.86 ± 0.02 upon increasing the $|V_{bias}|$ from 0 V up to the optimum condition (see the deconvolution of Hf 4f XPS spectrum in Figure AIVa-b). Interestingly, the high Hf(III) fraction achieved at the *optimum condition* for Ar–H_2 plasma is comparable to the previously reported H_2 plasma (i.e. 0.86 ± 0.02 vs. 0.82 ± 0.02).

Table 1 gives an overview of the material properties of HfN_x films grown at the *optimum condition* using Ar–H_2 plasma, whereas the film properties as a function of $|V_{bias}|$ can be found in the supporting information (Table AIII). The aforementioned increase in Hf(III) fraction upon increasing the $|V_{bias}|$ from 0 to 255 V is correlated with a major suppression in O content from 19.9 ± 0.9 at.% to <2 at.%. In our previous report on H_2 plasma [14], we also concluded that this increase in Hf(III) fraction with $|V_{bias}|$ is associated with a major decrease in O content in the HfN_x films. Additionally, the H content (and presumably Hf–H bonds) at the optimum condition appears to limit the Hf(III) fraction from reaching unity [14]. The latter suggestion is further corroborated by the fact that an increase in $|V_{bias}|$ beyond the *optimum condition* leads to an increase in H at.%, while a simultaneous decrease in Hf(III) fraction is observed (Table AIII). It should be noted that the O content stays below <2 at.% at $|V_{bias}|$ of 255 V or higher. Furthermore, the C concentration was found to increase upon increasing the $|V_{bias}|$ up to the optimum condition (see supporting information Figure AIVd). This increase in carbon is similar to previously reported H_2 plasma process and is thought to arise from enhanced cracking of ligands on the film surface by energetic ions, followed by their re-deposition [14, 30].

Based on these results, it can be concluded that a high Hf(III) fraction and a very low O content is achieved at the *optimum condition* for the HfN_x films grown using Ar–H_2 plasma, which is comparable to the previously reported H_2 plasma process.

Microstructural Properties of HfN_x

The crystallinity and microstructure of the HfN_x films were also investigated. In fact, we have previously shown that the ρ_e is also related to the film microstructure [14]. The crystallinity of 35 nm thick film grown using Ar–H_2 plasma and 80 nm thick film grown using H_2 plasma was examined using XRD ($\theta - 2\theta$ mode) (supporting information, Figure AV). Conducting δ-HfN phase was observed for the *optimum condition* of the Ar–H_2 plasma, exhibiting HfN(111), HfN(200) and HfN(220) reflections in a similar peak intensity ratio as the powder δ-HfN pattern [14], indicating no preferred growth direction.

The lateral grain sizes of the HfN_x films were subsequently investigated. Figure 3 shows top-view high-angle annular dark-field scanning transmission electron microscopy (HAADF-STEM) and scanning electron microscopy (SEM) images of HfN_x layers grown at the *optimum condition* of Ar–H_2 plasma, allowing evaluation of the lateral grain size as a function of film thickness. The images for H_2 plasma process are also shown for comparison purposes. It can be concluded from the data in HAADF-STEM and SEM images that the rate of lateral grain growth is higher for Ar–H_2 plasma as compared to the H_2 plasma

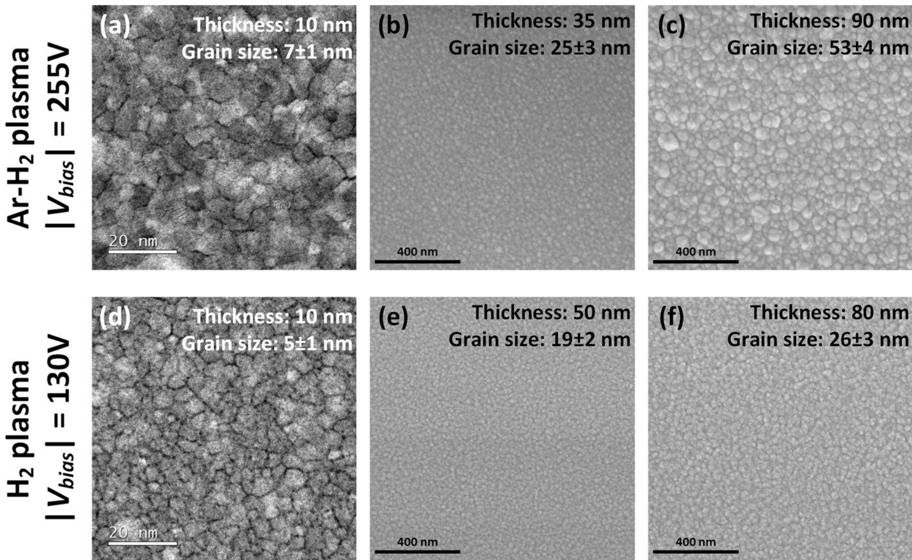

Fig. 3 Top-view high-angle annular dark-field scanning transmission electron microscopy (HAADF-STEM) and scanning electron microscopy (SEM) images for HfN_x films prepared at the *optimum conditions* using Ar–H_2 plasma and H_2 plasma with an approximate thickness of (**a**, **d**) 10 nm; (**b**, **e**) 35 nm and 50 nm; (**c**,**f**) 90 nm and 80 nm, respectively

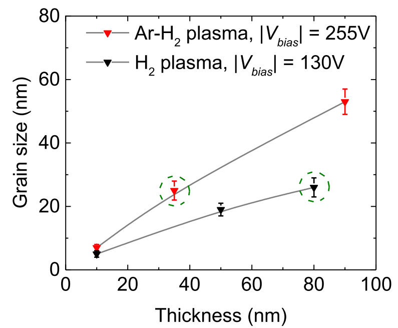

Fig. 4 Lateral grain sizes for the HfN_x films prepared at the *optimum conditions* of the Ar–H_2 plasma and H_2 plasma as a function of film thickness. The points with the (green) circles indicate the grain sizes of HfN_x films that are discussed in more detail in terms of resistivity for the corresponding ALD process (Color figure online)

(Fig. 4). Importantly, the lateral grain size for the relevant ~ 35 nm thick film grown using the Ar–H_2 plasma is similar to that of previously reported ~ 80 nm thick HfN_x film prepared with H_2 plasma (green circles in Fig. 4).

The in-grain crystal quality of the HfN_x films grown at the optimum conditions was investigated by studying its micro-structure. Figure 5 shows the HAADF-STEM image of cross-sectional samples for the Ar–H_2 plasma (35 nm thick) and the H_2 plasma (80 nm thick) cases. Dark regions in the films indicate the presence of lighter elements and/or porosity. The images with a 50 nm scale display the lateral development of crystal grains as a function of height, yielding similar grain size values on the top surfaces of the film as measured from the aforementioned top-view HAADF-STEM and SEM studies of Fig. 3. The higher magnification insets reveal that the HfN_x film grown using Ar–H_2 plasma are quite dense, i.e. displaying much less nano-porosity than the case of H_2 plasma. Specifically, non-uniform contrast variations and dark patches can be observed within the crystal

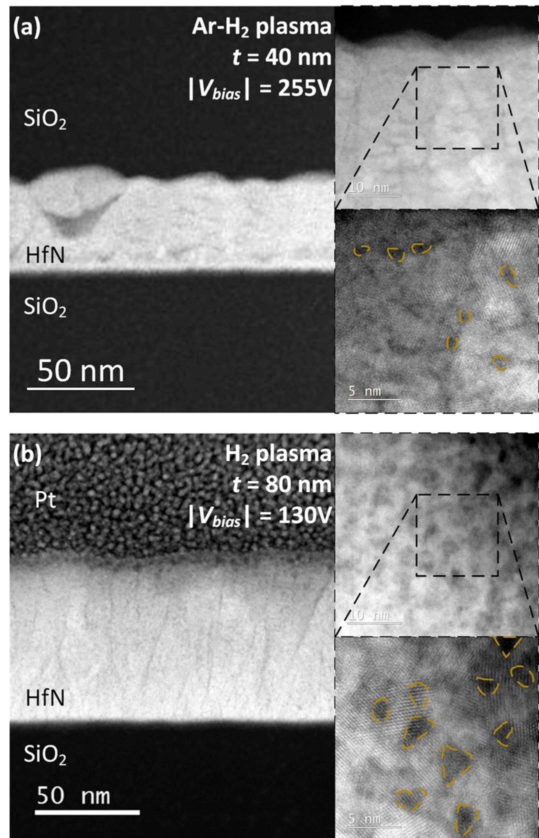

Fig. 5 Cross-sectional high-angle annular dark-field scanning transmission electron microscopy (HAADF-STEM) images for **a** ~ 35 nm thick film grown at $|V_{bias}|$= 255 V using Ar–H_2 plasma and **b** ~ 80 nm thick film prepared using H_2 plasma at $|V_{bias}|$= 130 V. The insets show magnified views of the micro-structure displaying the nano-scale porosity in the film as indicated by the highlighted (yellow) areas (Color figure online)

grains of the HfN_x film grown using H_2 plasma, suggesting the presence of lower density regions such as nano-pores. These results agree with the higher mass density obtained for HfN_x films grown using Ar–H_2 plasma in comparison with the H_2 plasma (Table 1).

In addition, we observed the presence of V-shaped pyramidal voids for the Ar–H_2 plasma in the initial phase of film growth (Fig. 5a). The cause for this phenomenon is not known yet. Although the voids can be observed in several areas of the whole TEM cross-section of the Ar–H_2 sample (supporting information, Figure AVI), it appears that their presence does not affect the film electrical properties.

Discussion and Conclusions

Plasma-assisted ALD of HfN_x has been studied using $CpHf(NMe_2)_3$ as the Hf(IV) precursor and Ar–H_2 plasma in combination with an external RF substrate bias application as the co-reactant. Ion energy characterization reveals that the average energy of the impinging ions ($<E_{ion}>$) on the HfN_x surface at the *optimum condition* of the lowest film resistivity of 4.1×10^{-4} Ωcm for Ar–H_2 plasma is 304 eV and the ion flux (Γ_i) is $(9.0 \pm 2.1)\cdot 10^{14}$ cm^{-2} s^{-1}. Such a low resistivity is achieved for films as thin as ~ 35 nm. From the extensive thin film characterization, we show that a very low O content (< 2 at.%)

Table 1 Properties of the HfN_x films prepared at *optimum conditions* using an Ar-H_2 plasma compared with previously reported properties of HfN_x films deposited using a H_2 plasma

Plasma $\|V_{bias}\|$ (V)	FPP	SE		XPS	RBS				ERD
	Electrical resistivity (Ωcm)	Optical resistivity (Ωcm)	Thickness (nm)	$\frac{Hf(III)}{Hf(III)+Hf(IV)}$	N/Hf	C (at.%)	O (at.%)	Mass density (g cm^{-3})	H (at.%)
Ar–H_2 255 V	4.1×10^{-4}	2.4×10^{-4}	35	0.86 ± 0.02	0.84 ± 0.08	8.4 ± 0.4	<2.0	10.0 ± 0.3	11.8 ± 0.6
H_2 130 V	3.3×10^{-3}	9.0×10^{-4}	80	0.82 ± 0.02	1.00 ± 0.07	11.0 ± 1.2	<2.0	8.6 ± 0.2	12.6 ± 0.6

The electrical resistivity was obtained by a combination of four-point probe (FPP) and spectroscopic ellipsometry (SE) whereas the optical resistivity and thickness were determined using SE. X-ray photoelectron spectroscopy (XPS) was used to obtain the Hf(III) oxidation state fraction whereas the chemical composition was determined via Rutherford backscattering (RBS). The H content was measured using elastic recoil detection (ERD). The mass density was calculated by dividing the total areal mass density (obtained via RBS and ERD) with the film thickness. The measurement errors for electrical and optical resistivities are less than 3% and 2% of their absolute values, respectively

and a correlated high Hf(III) oxidation state fraction of 0.86 ± 0.02 is obtained for the HfN_x films grown at the *optimum condition*. Furthermore, the HfN_x films exhibit a very low in-grain nano-porosity. The high in-grain crystalline quality and low in-grain nano-porosity is also in line with the aforementioned observation on the very low electronic scattering (i.e. small $\Delta\rho$) in the HfN_x films (Fig. 2a). Altogether, these excellent material properties lead to the very low ρ_e of the HfN_x films grown using Ar–H_2 plasma with energetic ion bombardment.

Impinging ions during plasma processes are known to initiate several interactions with the growing films, for example, enhanced ad atom surface diffusion leading to decrease in the defect density; bulk lattice atom displacements resulting in a collision cascade; sputtering and ion-induced damage; ion implantation at higher ion energies [20, 43–51]. In regards to the material properties, Hultman et al. and Petrov et al. showed that energetic ions in a N_2 and Ar–N_2 plasma discharges respectively with $|V_{bias}|$ value in the range of 150 V—250 V can lead to annihilation of defects and reduction in nano-porosity in sputtered TiN films [52, 53], and attributed the decrease in defect density to the near-surface and sub-surface diffusion processes [44, 45].

Next to the ion energy, the mass of impinging ions is of importance. In our case, from the ion energy results and from literature reports [28], it is concluded that the HfN_x film surface at the *optimum conditions* is subjected to energetic ions with significantly higher ion energy and larger mass when using an Ar–H_2 plasma (mainly ArH^+) instead of a H_2 plasma ($<E_{ion}> = 159$ eV, mainly H_3^+), while the Γ_i remains comparable ($\Gamma_i = (8.2 \pm 1.9) \cdot 10^{14}$ cm^{-2} s^{-1} for H_2 plasma). It is further noted that the ρ_e value for HfN_x films grown at the *optimum conditions* using Ar–H_2 plasma is an order of magnitude lower than the H_2 plasma. This major decrease in the ρ_e value is primarily attributed to the improvement in the HfN_x film microstructure, enabled by the impingement of ions with a larger mass and higher energy. Relevantly, Villamayor et al. also recently showed that an increase in the mass of impinging ions by adopting Kr–N_2 plasma, instead of Ar–N_2 plasma, led to an improvement in the crystalline quality of the sputtered HfN_x films [20]. The above results can be understood from the fact that the nature of ion-surface interaction depends on the extent of energy and momentum transfer. As highlighted by Gago et al. [48], the system can be approximated by the simple case of an elastic binary atom(ion)-atom collision. Using this model, the kinematic factor (k) for energy transfer can be easily calculated using $k = 4Mm\big/(M+m)^2 \cdot cos^2\varphi$, where M and m are the masses of incoming ion and target atom respectively and φ is the scattering angle [48]. It should be noted that the value of k is approximately an order of magnitude higher for the impinging heavy ArH^+ ions in comparison to the light H_3^+ ions, when Hf is considered as the target atom. Altogether, it is expected that the impinging ions with a higher energy (304 vs. 159 eV) and larger mass (ArH^+ vs. H_3^+) may lead to a greater extent of energy and momentum transfer to the HfN_x film surface [20, 43–51].

In addition to the higher energy and larger momentum transfer of ArH^+ ions, it should also be noted that ArH^+ ions are expected to have a smaller penetration depth than H_3^+ ions. This signifies that the energy and momentum transfer per ALD cycle using ArH^+ ions occurs primarily in a shallower region of the film. Therefore, the energy density available to promote the decrease in nanoporosity is higher when using ArH^+ ions. So to conclude, the obtained results demonstrate how energy density and mass of impinging ions and the associated energy and momentum transfer during plasma ALD can contribute to the fine tuning of the chemical and microstructural properties of HfN_x thin films. The results may be applicable to wide range of ALD processes including for the growth of other transition metal nitrides [54].

Supporting Information

Substrate potential via oscilloscope, GPC as a function of $|V_{bias}|$, SE modeling parameters for HfN_x, HfN_x material property as a function of $|V_{bias}|$, XPS spectra for Hf 4f, O 1 s and C 1 s as a function of $|V_{bias}|$, θ-2θ XRD scan and HAADF-STEM image for HfN_x film strip.

Acknowledgments The authors thank Dr. Vincent Vandalon, Dr. Richard Engeln and Dr. Harm Knoops (University of Technology Eindhoven) for fruitful discussions and Cristian van Helvoirt and Jeroen van Gerwen (University of Technology Eindhoven) for the skillful technical assistance. Dr. Beatriz Barcones Campo (University of Technology Eindhoven) is acknowledged for the FIB preparation of the TEM samples. Solliance and the Dutch province of Noord-Brabant are acknowledged for funding the TEM facility. The authors would also like to thank Vivek Beladiya (University of Jena) for the stress measurements. This work was supported financially by Technologiestichting STW through the project LIMIET (#13316) and Netherlands Organization for Scientific Research NWO through project HTSM (#15352). Air Liquide is kindly acknowledged for providing the Hf precursor.

Author Contributions All authors have given approval to the final version of the manuscript.

Compliance with ethical standards

Conflict of interest The authors declare no competing financial interest.

Open Access This article is licensed under a Creative Commons Attribution 4.0 International License, which permits use, sharing, adaptation, distribution and reproduction in any medium or format, as long as you give appropriate credit to the original author(s) and the source, provide a link to the Creative Commons licence, and indicate if changes were made. The images or other third party material in this article are included in the article's Creative Commons licence, unless indicated otherwise in a credit line to the material. If material is not included in the article's Creative Commons licence and your intended use is not permitted by statutory regulation or exceeds the permitted use, you will need to obtain permission directly from the copyright holder. To view a copy of this licence, visit http://creativecommons.org/licenses/by/4.0/.

References

1. Liu Y, Nabatame T, Nguyen N, Matsukawa T, Endo K, O'Uchi S, Tsukada J, Yamauchi H, Ishikawa Y, Mizubayashi W, Morita Y, Migita S, Ota H, Chikyow T, Masahara M (2015) Channel shape and interpoly dielectric material effects on electrical characteristics of floating-gate-type three-dimensional fin channel flash memories. Jpn J Appl Phys. https://doi.org/10.7567/JJAP.54.04DD04
2. Pierson HO (1996) Handbook of Refractory Carbides and Nitrides: Properties, Characteristics Processing and Apps. Elsevier Science, Amsterdam
3. Franklin AD, Koswatta SO, Farmer DB, Smith JT, Gignac L, Breslin CM, Han S-J, Tulevski GS, Miyazoe H, Haensch W, Tersoff J (2013) Carbon s. Nano Lett 13(6):2490–2495. https://doi.org/10.1021/nl400544q
4. Yu HY, Li MF, Kwong DL (2004) Thermally robust HfN metal as a promising gate electrode for advanced MOS device applications. IEEE Trans Electron Devices 51(4):609–615. https://doi.org/10.1109/TED.2004.825110
5. Hu CK, Harper JME (1998) Copper interconnections and reliability. Mater Chem Phys 52(1):5–16. https://doi.org/10.1016/S0254-0584(98)80000-X
6. Jeong W, Ko Y, Bang S, Lee S, Jeon H (2010) Characteristics of HfN films deposited by using remote plasma-enhanced atomic layer deposition. J Korean Phys Soc 56(3):905–910
7. Kim H, Cabral C, Lavoie C, Rossnagel SM (2002) Diffusion barrier properties of transition metal thin films grown by plasma-enhanced atomic-layer deposition. J Vac Sci Technol B Microelectron Nanometer Struct 20(4):1321–1326. https://doi.org/10.1116/1.1486233

8. Yu HY, Kang JF, Ren C, Chen JD, Hou YT, Shen C, Li MF, Chan DSH, Bera KL, Tung CH, Kwong DL (2004) Robust high-quality HfN-HfO 2 Gate stack for advanced MOS device applications. IEEE Electron Device Lett 25(2):70–72. https://doi.org/10.1109/LED.2003.820649
9. Xu M, Wang S, Yin G, Li J, Zheng Y, Chen L, Jia Y (2006) Optical properties of cubic Ti3N4, Zr3N4, and Hf3N4. Appl Phys Lett. https://doi.org/10.1063/1.2360937
10. Becker JS, Kim E, Gordon RG (2004) Atomic layer deposition of insulating hafnium and zirconium nitrides. Chem Mater 16(18):3497–3501. https://doi.org/10.1021/cm049516y
11. Hu C, Gu Z, Wang J, Zhang K, Zhang X, Li M, Zhang S, Fan X, Zheng W (2014) Nature of tunable optical reflectivity of rocksalt hafnium nitride films. J Phys Chem C 118(35):20511–20520. https://doi.org/10.1021/jp504004e
12. Farrell IL, Reeves RJ, Preston ARH, Ludbrook BM, Downes JE, Ruck BJ, Durbin SM (2010) Tunable electrical and optical properties of hafnium nitride thin films. Appl Phys Lett. https://doi.org/10.1063/1.3327329
13. Karwal S, Williams BL, Niemelä JP, Verheijen MA, Kessels WMM, Creatore M (2017) Plasma-assisted atomic layer deposition of HfNx: Tailoring the film properties by the plasma gas composition. J Vac Sci Technol A Vac Surf Films. https://doi.org/10.1116/1.4972208
14. Karwal S, Verheijen MA, Williams BL, Faraz T, Kessels WMM, Creatore M (2018) Low resistivity HfNx grown by plasma-assisted ALD with external RF substrate biasing. J Mater Chem C 6(15):3917–3926. https://doi.org/10.1039/C7TC05961B
15. Knoops HCM, Langereis E, Sanden MCMVD, Kessels WMM (2012) Reaction mechanisms of atomic layer deposition of TaNx from Ta(NMe2)5 precursor and H2-based plasmas. J Vac Sci Technol, A 30(1):01A101. https://doi.org/10.1116/1.3625565
16. Johansson BO, Helmersson U, Hibbs MK, Sundgren JE (1985) Reactively magnetron sputtered Hf-N films. I. Composition and structure. J Appl Phys 58(8):3104–3111. https://doi.org/10.1063/1.335812
17. Johansson BO, Sundgren JE, Helmersson U (1985) Reactively magnetron sputtered Hf-N films. II. Hardness and electrical resistivity. J Appl Phys 58(8):3112–3117. https://doi.org/10.1063/1.335813
18. Seo HS, Lee TY, Wen JG, Petrov I, Greene JE, Gall D (2004) Growth and physical properties of epitaxial HfN layers on MgO(001). J Appl Phys 96(1):878–884. https://doi.org/10.1063/1.1759783
19. Shinkai S, Sasaki K (1999) Influence of sputtering parameters on the formation process of high-quality and low-resistivity HfN thin film. Jpn J Appl Phys Part 1 Regul Pap Short Note Rev Pap 38(4):2097–2102
20. Villamayor MMS, Keraudy J, Shimizu T, Viloan RPB, Boyd R, Lundin D, Greene JE, Petrov I, Helmersson U (2018) Low temperature (Ts/Tm %3c 0.1) epitaxial growth of HfN/MgO(001) via reactive HiPIMS with metal-ion synchronized substrate bias. J Vac Sci Technol A 36(6):061511. doi:10.1116/1.5052702
21. Kim Y, Baunemann A, Parala H, Devi A, Fischer RA (2005) Metal-organic CVD of conductive and crystalline hafnium nitride films. Chem Vapor Deposition 11(6–7):294–297. https://doi.org/10.1002/cvde.200504204
22. Consiglio S, Zeng W, Berliner N, Eisenbraun ET (2008) Plasma-assisted atomic layer deposition of conductive hafnium nitride using tetrakis(ethylmethylamino)hafnium for CMOS gate electrode applications. J Electrochem Soc 155(3):H196–H201. https://doi.org/10.1149/1.2827995
23. Kim EJ, Kim DH (2006) Highly conductive HfN x films prepared by plasma-assisted atomic layer deposition. Electrochem Solid State Letters 9(8):C123–C125. https://doi.org/10.1149/1.2206884
24. Elam JW, Libera JA, Huynh TH, Feng H, Pellin MJ (2010) Atomic layer deposition of aluminum oxide in mesoporous silica gel. J Phys Chem C 114(41):17286–17292. https://doi.org/10.1021/jp1030587
25. Haukka S, Lakomaa E-L, Julha O, Vilhunen J, Hornytzkyj S (1993) Dispersion and distribution of titanium species bound to silica from TiCl4. Langmuir 9(12):3497–3506
26. Lakomaa EL, Root A, Suntola T (1996) Surface reactions in Al2O3 growth from trimethylaluminium and water by atomic layer epitaxy. Appl Surf Sci 107:107–115. https://doi.org/10.1016/s0169-4332(96)00513-2
27. Keranen J, Guimon C, Iiskola E, Auroux A, Niinisto L (2003) Surface-controlled gas-phase deposition and characterization of highly dispersed vanadia on silica. J Phys Chem B 107(39):10773–10784
28. Sode M, Schwarz-Selinger T, Jacob W (2013) Ion chemistry in H2-Ar low temperature plasmas. J Appl Phys 114 (6). https://doi.org/10.1063/1.4817526
29. Knoops HCM, Braeken EMJ, De Peuter K, Potts SE, Haukka S, Pore V, Kessels WMM (2015) Atomic layer deposition of silicon nitride from Bis(tert-butylamino)silane and N%3cinf%3e2%3c/

inf%3e Plasma. ACS Appl Mater Interfaces 7(35):19857–19862. https://doi.org/10.1021/acsami.5b06833

30. Knoops HCM, De Peuter K, Kessels WMM (2015) Redeposition in plasma-assisted atomic layer deposition: silicon nitride film quality ruled by the gas residence time. Appl Phys Lett. https://doi.org/10.1063/1.4926366
31. Profijt HB, Van De Sanden MCM, Kessels WMM (2013) Substrate-biasing during plasma-assisted atomic layer deposition to tailor metal-oxide thin film growth. J Vac Sci Technol A Vac Surf Films. https://doi.org/10.1116/1.4756906
32. Gahan D, Daniels S, Hayden C, Scullin P, O'Sullivan D, Pei YT, Hopkins MB (2012) Ion energy distribution measurements in RF and pulsed dc plasma discharges. Plasma Sour Sci Technol. https://doi.org/10.1088/0963-0252/21/2/024004
33. Gahan D, Dolinaj B, Hopkins MB (2008) Retarding field analyzer for ion energy distribution measurements at a radio-frequency biased electrode. Rev Sci Instrum. https://doi.org/10.1063/1.2890100
34. Faraz T, Arts K, Karwal S, Knoops HCM, Kessels WMM (2019) Energetic ions during plasma-enhanced atomic layer deposition and their role in tailoring material properties. Plasma Sour Sci Technol 28(2):024002. https://doi.org/10.1088/1361-6595/aaf2c7
35. Timofeeva II, Shvedova LK (1972) Microhardness and thermal expansion of transition metal nitrides within the 80–300K temperature range. Izvestiya Akademii Nauk SSSR, Neorganicheskie Materialy 8(6):1169–1170
36. Wang W, Nabatame T, Shimogaki Y (2008) Preparation of conductive HfN by post rapid thermal annealing-assisted MOCVD and its application to metal gate electrode. Microelectron Eng 85(2):320–326. https://doi.org/10.1016/j.mee.2007.07.003
37. Rennick CJ, Engeln R, Smith JA, Orr-Ewing AJ, Ashfold MNR, Mankelevich YA (2005) Measurement and modeling of a diamond deposition reactor: hydrogen atom and electron number densities in an Ar/H2 arc jet discharge. J Appl Phys 97(11):113306. https://doi.org/10.1063/1.1906288
38. Meulenbroeks RFG, van Beek AJ, van Helvoort AJG, van de Sanden MCM, Schram DC (1994) Argon-hydrogen plasma jet investigated by active and passive spectroscopic means. Phys Rev E 49(5):4397–4406. https://doi.org/10.1103/PhysRevE.49.4397
39. Jiménez-Redondo M, Cueto M, Doménech JL, Tanarro I, Herrero VJ (2014) Ion kinetics in Ar/H2 cold plasmas: the relevance of ArH+. RSC advances 4(107):62030–62041. https://doi.org/10.1039/C4RA13102A
40. Manenschijn A, Janssen GCAM, Van Der Drift E, Radelaar S (1991) Measurement of ion impact energy and ion flux at the RF electrode of a parallel plate reactive ion etcher. J Appl Phys 69(3):1253–1262. https://doi.org/10.1063/1.347311
41. Adibi F, Petrov I, Greene JE, Hultman L, Sundgren JE (1993) Effects of high-flux low-energy 20–100 eV ion irradiation during deposition on the microstructure and preferred orientation of Ti0.5Al0.5N alloys grown by ultra-high-vacuum reactive magnetron sputtering. J Appl Phys 73(12):8580–8589. https://doi.org/10.1063/1.353388
42. Knoops HCM, van de Loo BWH, Smit S, Ponomarev MV, Weber J-W, Sharma K, Kessels WMM, Creatore M (2015) Optical modeling of plasma-deposited ZnO films: Electron scattering at different length scales. J Vac Sci Technol A 33(2):021509. https://doi.org/10.1116/1.4905086
43. Insepov Z, Yamada I, Sosnowski M (1998) Sputterring and smoothing of metal surface with energetic gas cluster beams. Mater Chem Phys 54(1):234–237. https://doi.org/10.1016/S0254-0584(98)00032-7
44. Wang LP, Fu KY, Tian XB, Tang BY, Chu PK (2002) Influence of temperature and ion kinetic energy on surface morphology of CeO2 films prepared by dual plasma deposition. Mater Sci Eng, A 336(1):75–80. https://doi.org/10.1016/S0921-5093(01)01923-2
45. Gottlieb SO, Satoshi H (2018) Foundations of low-temperature plasma enhanced materials synthesis and etching. Plasma Sour Sci Technol 27(2):023001
46. Nastasi M, Mayer J, Hirvonen JK (1996) Ion stopping. In: Ion-solid interactions: fundamentals and applications. Cambridge Solid State Science Series. Cambridge University Press, Cambridge, pp 88–114. https://doi.org/10.1017/CBO9780511565007.006
47. Insepov Z, Yamada I (1995) Molecular dynamics simulation of cluster ion bombardment of solid surfaces. Nucl Instrum Methods Phys Res, Sect B 99(1):248–252. https://doi.org/10.1016/0168-583X(95)00322-3
48. Gago R, Jiménez I, Albella J (2006) Thin film growth by ion-beam-assisted deposition techniques. Elesiver, Amsterdam, pp 345–382. https://doi.org/10.1016/B978-008044496-3/50011-3
49. Anders A (2010) A structure zone diagram including plasma-based deposition and ion etching. Thin Solid Films 518(15):4087–4090. https://doi.org/10.1016/j.tsf.2009.10.145

50. Auciello O, Kelly R (1984) Ion bombardment modification of surfaces: fundamentals and applications. Elsevier Science Publishers, Amsterdam
51. Greene JE, Barnett SA (1982) Ion-surface interactions during vapor phase crystal growth by sputtering, MBE, and plasma-enhanced CVD: applications to semiconductors. J Vac Sci Technol V 21(2):285–302
52. Hultman L, Helmersson U, Barnett SA, Sundgren JE, Greene JE (1987) Low-energy ion irradiation during film growth for reducing defect densities in epitaxial TiN(100) films deposited by reactive-magnetron sputtering. J Appl Phys 61(2):552–555. https://doi.org/10.1063/1.338257
53. Petrov I, Hultman L, Helmersson U, Sundgren JE, Greene JE (1989) Microstructure modification of TiN by ion bombardment during reactive sputter deposition. Thin Solid Films 169(2):299–314. https://doi.org/10.1016/0040-6090(89)90713-X
54. Faraz T, Knoops HCM, Verheijen MA, van Helvoirt CAA, Karwal S, Sharma A, Beladiya V, Szeghalmi A, Hausmann DM, Henri J, Creatore M, Kessels WMM (2018) Tuning material properties of oxides and nitrides by substrate biasing during plasma-enhanced atomic layer deposition on planar and 3D substrate topographies. ACS Appl Mater Interfaces 10(15):13158–13180. https://doi.org/10.1021/acsami.8b00183

Publisher's Note Springer Nature remains neutral with regard to jurisdictional claims in published maps and institutional affiliations.